



Optical flow estimations in aerated spillway flows: Filtering and discussion on sampling parameters

Matthias Kramer^{*}, Hubert Chanson

The University of Queensland, School of Civil Engineering, Brisbane, QLD 4072, Australia

ARTICLE INFO

Keywords:

Air-water flows
Stepped spillway
Phase-detection probe
Optical flow
Signal processing
Sampling parameters

ABSTRACT

Image-based velocimetry captured a great interest in physical modelling of highly-aerated flows, for example in stepped spillways. The present study investigated the performance of a novel filtering technique based upon a detailed systematic comparison with intrusive phase-detection probe data. All measurements were conducted in a large-size stepped spillway. A sensitivity analysis provided recommendations in terms of optimum sampling and processing parameters for optical flow measurements in high-velocity air-water flows.

1. Introduction

Measurement techniques for multiphase flows are different from monophasic flow methods as the flow field is characterised by additional quantities, for example the void fraction or the bubble/droplet count rate. To measure the characteristics of air-water flows, the deployed instrumentation must be applicable to quantify these parameters accurately within a wide range of void fraction levels, typically from nearly zero to unity in a spillway flow. Intrusive phase-detection probes (conductivity and optical fiber probes) constitute a thoroughly proven technique in physical modelling of high-velocity air-water flows [28,18,7,8].

Image-based velocimetry methods have captured great interest in the study of air-water flows as these methods are able to provide dense velocity fields with an information content exceeding traditional point-wise measurements. The bubble image velocimetry (BIV) is a modified particle image velocimetry (PIV) method and was first introduced by Ryu et al. [29]. Entrained air-bubbles are used to determine the velocity field by correlating textures within the bubbly flow images. Leandro et al. [24] used BIV to measure velocity fields within the aerated skimming flow regime of stepped spillways with different slopes. The obtained velocities were in general agreement with intrusive phase-detection measurements at the centreline of the channel, although showing a persistent underestimation. Sidewall effects and measurement uncertainties explained the result. Kramer and Chanson [22] were the first using particle tracking velocimetry (PTV) to characterise free-surface instabilities in air-water flows next to the inception point of self-aeration.

An alternative image-based approach is the class of optical flow (OF) methods. Optical flow refers to the apparent velocity vector field corresponding to the observed displacement of intensity patterns in successive image sequences [17,15]. Optical flow methods are classified into local methods, such as the Lucas/Kanade technique [27], and into global techniques as the Horn/Schunck approach [19]. For general information on optical flow algorithms, the reader is referred to the following references, which include performance evaluations of different optical flow techniques [1,16], first applications of optical flow techniques to fluid flows [10,26] and a comparison between optical flow and cross-correlation methods [25].

In the field of air-water flows, Bung and Valero [3,5] applied OF and BIV to the skimming flow regime of a stepped spillway. The optical flow method gave velocity data with the same or even higher accuracy when compared to BIV. A comparison with phase-detection conductivity probe data (recorded at the centreline of the channel) revealed an increasing deviation of the streamwise velocity in regions with high void fractions for both image-based methods. Homogeneous pixel intensity with low intensity gradients and strong blurring were believed to cause this deviation. Zhang and Chanson [32] conducted validation tests for optical flow techniques using a dual-tip phase-detection conductivity probe (CP) mounted next to the sidewall. The streamwise optical flow velocities were in agreement with the phase-detection probe measurements at low void fractions, whereas increasing differences were observed for void fractions $C > 0.5$. It was found that the optical flow estimates were sensitive to velocity gradients and the video sampling rate.

Table 1 summarises laboratory investigations on image based-

^{*} Corresponding author.

E-mail addresses: m.kramer@uq.edu.au (M. Kramer), h.chanson@uq.edu.au (H. Chanson).

Table 1

Image based velocity measurements in aerated spillway flows; BIV: bubble image velocimetry; OF: optical flow; CP: conductivity probe; VC: high-speed video camera.

Reference	θ [°]	W [m]	q [m ² /s]	d_c/h [–]	Method
Leandro et al. [24]	18.4; 26.6	0.3	0.07 to 0.11	1.3 to 3.6	BIV
Bung and Valero [3]	26.6	0.3; 0.5	0.07	1.3	BIV/OF
Bung and Valero [5]	26.6	0.5	0.07	1.3	OF
Zhang and Chanson [32]	45.0	0.985	0.083	0.9	OF
Current study	45.0	0.985	0.067	0.8	OF

Reference	$f_{s,OF}$ [kHz]	$t_{s,OF,max}$ [s]	ρ_{px} [px/cm]	Instrumentation
Leandro et al. [24]	1.2	1.0	12–16	CP (center), VC
Bung and Valero [3]	0.7–1.2	1.3	14–103	CP (center), VC
Bung and Valero [5]	0.7	0.3	103	CP (center), VC
Zhang and Chanson [32]	0.5–10.0	15.0	36	CP (sidewall), VC
Current study	0.5–20.0	20.0	25–35	CP (multiple locations), VC

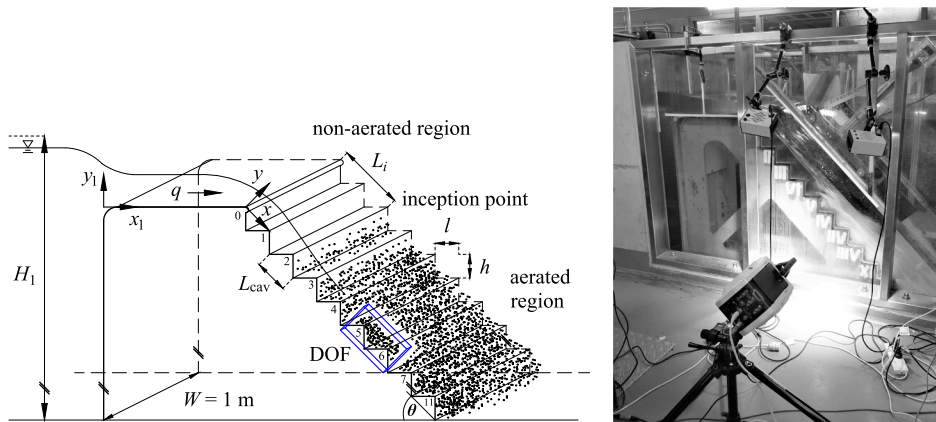


Fig. 1. Experimental setup. (A, left) Definition sketch of the broad crested weir and the stepped spillway; l : step length; h : step height; L_{cav} : cavity length; W : channel width; θ : spillway slope; x : longitudinal direction; y : vertical direction; H_1 : upstream head; q : specific discharge; L_i : inception point location; note the indicated OF measurement location (blue window); DOF: depth of field. (B, right) Alignment of the high-speed video camera in front of the physical spillway model; flow direction from top left to bottom right; camera rotated by 45°. (For interpretation of the references to colour in this figure legend, the reader is referred to the web version of this article.)

velocimetry in aerated spillway flows, together with the experimental conditions of the present study. Herein, θ is the channel slope (Fig. 1A), W is the channel width, q is the specific water discharge, $f_{s,OF}$ is the video sampling frequency, $t_{s,OF}$ is the video sampling duration, ρ_{px} is the pixel density and d_c/h is the dimensionless flow rate, where d_c is the critical depth $d_c = (q^2/g)^{1/3}$, h is the vertical step height and g is the gravitational acceleration.

Since the application of image-based techniques is relatively new in the study of air-water flows, the validation of optical flow methods and sensitivity analyses of key sampling and processing parameters are important. A first step must assess low-order flow statistics to provide the basis for further development, which could then be used to identify turbulent scales and flow structures. In this context, velocity statistics are most relevant as they can directly be compared to phase-detection probe measurements.

The aim of this study is to improve the interpretation of image-based velocimetry data in high-velocity air-water flows. A novel filtering technique is presented, together with a thorough validation of optical flow measurements in a large-size stepped spillway. The results and discussion sections include intrusive phase-detection probe measurements at different longitudinal and transverse locations (Section 4.1), optical flow measurements (Section 4.2), a validation of optical flow velocity estimates (Section 5.1) and a systematic investigation of key sampling and processing parameters (Section 5.2). The sensitivity analysis provided useful recommendations for future measurements.

2. Experimental setup and instrumentation

2.1. Experimental facility

Experiments were conducted in a large-size physical model of a steep stepped spillway with a slope of $\theta = 45^\circ$. The physical model of the chute was 0.985 m wide and had 12 steps with a step length of $l = 0.1$ m and a step height of $h = 0.1$ m. The step edges were increasingly numbered and step edge 0 corresponded to the rounded downstream edge of the broad crested weir (Fig. 1A). All other step edges were sharp-edged. The inflow conditions were quasi-uniform due to a large inlet basin equipped with a multitude of longitudinal flow straighteners. Further details of the physical model, e.g. concerning the geometry of the inlet section or on the operation of the weir crest, were published in Zhang and Chanson [31] and Kramer and Chanson [23]. A trolley was mounted parallel to the pseudo-bottom (formed by the step edges) of the spillway chute and allowed for the positioning of phase-detection probes at different longitudinal and transverse positions.

2.2. Instrumentation

The present instrumentation included intrusive and non-intrusive measurement techniques. Clear-water flow depths in the non-aerated region of the chute were measured with two pointer-gauges, located at $x_i/L_{crest} = -0.92$ (upstream section) and $x_i/L_{crest} = 0.5$ (middle of the weir crest). The pointer-gauges were mounted at the centreline of the channel and had an accuracy of ± 1 mm [31].

A dual-tip phase-detection conductivity probe (inner diameter: 0.25 mm, outer diameter: 0.8 mm, longitudinal tip separation $\Delta x = 4.7$ mm) was used to measure air-water flow properties at different longitudinal and transverse locations of the stepped chute. The sampling rate ($f_{s,CP}$) and duration ($t_{s,CP}$) were 20 kHz and 90 s, respectively. The choice of the sampling parameters fulfilled the requirements set by earlier sensitivity analyses, e.g. Toombes [30] and Felder and Chanson [14].

The image sequences of the air-water flow down the spillway were filmed using a Phantom v2011 high-speed video camera (Fig. 1B). The camera was set up at a distance of around 1 m to the sidewall and was aligned with the pseudo-bottom of the spillway (corresponds to a rotation of 45°). The camera was equipped with an AF Nikkor 50 mm lens, which allowed for the recording of images with a small degree of distortion. A uniform illumination of the flow was achieved by attaching two 4x6 high power LED lamps (GS Vitec MultiLED) to the frame of the spillway model (Fig. 1B). Note that the LED lamps were not synchronised with the camera, but preliminary investigations showed that potential effects were negligible. The camera was focused on the flow next to the sidewall and the depth of field (DOF) was approximately stretching within 3 mm from the inside wall. Information beyond the DOF was potentially collected in form of blurred background motion and a so-called indicator function was implemented to filter interfacial foreground features.

The signal was recorded at video sampling durations ranging from $t_{s,OF} = 6.9$ s to 20 s and video sampling rates $f_{s,OF} = 5$ kHz and 20 kHz with HD resolution (1280 × 800 pixels, Table 2). Videos were recorded with two different pixel densities ($\rho_{px} = 25$ px/cm and 35 px/cm) because the camera's internal storage capacity was restricted. Sensitivity analyses were performed on sub-sampled and segmented signals (Table 2).

2.3. Investigated flow conditions

The experiments were conducted for a dimensionless discharge $d_c/h = 0.8$ within the upper transition flow regime. The transition flow regime occurred at intermediate discharges and was characterised by falling nappes and recirculation water pools within the step cavities. The impacting nappes generated strong hydrodynamic fluctuations and intense splashing next to the air-water surface. Based on different void fraction profiles (straight and flat versus S-shaped curvature), a lower (TRA1) and an upper (TRA2) sub-regime of the transition flow could be distinguished [9]. A turbulent shear-layer was forming in the wake of the step edges. Note that a recent study of Kramer and Chanson [23] presented detailed two-phase flow measurements at various flow rates ($d_c/h = 0.5$ –0.8) within both transition flow sub-regimes.

The specific discharge of the performed experiments was $q = 0.067$ m²/s (TRA2), which corresponded to a Reynolds number of $Re = 4q/\nu = 2.7 \times 10^5$, where ν is the kinematic viscosity of water. The slope of the chute was $\theta = 45^\circ$ and the inception point was visually determined at $L_i/L_{cav} = 2.0$, where L_i indicates the longitudinal distance from the downstream end of the weir and L_{cav} is the cavity length ($L_{cav} = \sqrt{2} \times 0.1$ m).

3. Signal processing

3.1. Phase-detection probe signals

Intrusive phase-detection conductivity probes are designed to pierce

Table 2
Sampling parameters of recorded image sequences.

Section	$f_{s,OF}$ [kHz]	$t_{s,OF}$ [s]	ρ_{px} [px/cm]	Comment
4.2; 5.2.3	5	11.8	35	
5.2.1	20	6.9	25	Sub-sampling
5.2.2	5	20	25	Segmentation

bubbles and droplets in air-water flows and different resistivities allow for the determination of air-water flow properties [28,20,18].

A detailed description of the typical raw-voltage output of a dual-tip phase-detection probe and the subsequent signal processing is given in Felder and Chanson [14]. Basic two-phase flow parameters include void fraction (C), bubble count rate (F) and interfacial velocity (V_x). Herein, the void fraction was determined based on a single-threshold technique [7] and the bubble count rate was equal to half the number of air-water interfaces detected per unit time. Cross-correlation analyses yielded the time delay between the leading and trailing tip signals, allowing for an estimation of the interfacial velocity.

Cummings and Chanson [11] and Boes [2] assessed the interfacial velocity uncertainty of intrusive phase-detection probes (conductivity and fiber-optical probes) to be within $\pm 5\%$. In the present study, the error of measured time-averaged air-water velocities was estimated as follows: $\Delta V_x/V_x < 5\%$ for $0.05 < C < 0.95$ and $\Delta V_x/V_x < 10\%$ for $0.01 < C < 0.05$ and $0.95 < C < 0.99$.

3.2. Video signals

3.2.1. Optical flow algorithm

The signals of the high-speed video camera were processed with the optical flow method. Optical flow refers to a non-intrusive image-based velocimetry technique and relies on the movement of brightness intensity patterns through an image sequence. In this study, the flow was recorded from a sidewall perspective and the connection between air-water flow and optical flow was straightforward under the assumption that (1) the flow was parallel to the sidewall and that (2) the out-of-plane component was zero. The two-dimensional optical flow was estimated based on the local Farnebaeck method [13], implemented in Matlab R2017b. The idea behind this method is to approximate the pixel intensity in some neighbourhood of each pixel with quadratic polynomials

$$I_1(x, y) = \mathbf{x}^T \mathbf{A}_1 \mathbf{x} + \mathbf{b}_1^T \mathbf{x} + c_1 \quad (1)$$

where I is the pixel intensity, \mathbf{x} is the coordinate vector, \mathbf{A}_1 is a symmetric matrix, \mathbf{b}_1 is a vector, c_1 is a scalar and the index 1 refers to the first image of an image pair. After a shift of the signal by a displacement \mathbf{d} , the pixel intensity pattern of the second image can be constructed as follows

$$I_2(x, y) = I_1(\mathbf{x} - \mathbf{d}) = (\mathbf{x} - \mathbf{d})^T \mathbf{A}_1 (\mathbf{x} - \mathbf{d}) + \mathbf{b}_1^T (\mathbf{x} - \mathbf{d}) + c_1 \quad (2)$$

$$= \mathbf{x}^T \mathbf{A}_1 \mathbf{x} + (\mathbf{b}_1 - 2\mathbf{A}_1 \mathbf{d})^T \mathbf{x} + \mathbf{d}^T \mathbf{A}_1 \mathbf{d} - \mathbf{b}_1^T \mathbf{d} + c_1 \quad (3)$$

$$= \mathbf{x}^T \mathbf{A}_2 \mathbf{x} + \mathbf{b}_2^T \mathbf{x} + c_2 \quad (4)$$

A comparison of the polynomial coefficients of Eqs. (3) and (4) yields an expression for the displacement vector [13]

$$2\mathbf{A}_1 \mathbf{d} = -(\mathbf{b}_2 - \mathbf{b}_1) \quad (5)$$

$$\mathbf{d} = -\frac{1}{2} \mathbf{A}_1^{-1} (\mathbf{b}_2 - \mathbf{b}_1) \quad (6)$$

The direct comparison of the polynomial coefficients implies a conservation of the pixel intensity (also known as brightness constancy constraint), expressed by $\mathbf{A}_1 = \mathbf{A}_2$. As this is most likely not the case in practical applications, the global polynomial might be replaced with local polynomials, leading to an approximation of the symmetric matrix: $\mathbf{A}(x) = (\mathbf{A}_1(x) + \mathbf{A}_2(x))/2$. Further, Eq. (6) can be solved pointwise but the results might be too noisy [13]. Therefore, the pixel-wise solution was integrated over a specified neighbourhood-size, assuming that there is only little variation in the displacement field within the specified area. Further details on the method are given in Farnebaeck [12,13].

3.2.2. Indicator function

An error propagation for optical flow computations was examined in Liu and Shen [26]. It was shown that the optical flow error mainly depends on the time interval between two consecutive images and on the image intensity gradient. For a given value of the time interval, a larger intensity gradient leads to a smaller error in the optical flow result [26].

As the recorded image sequences were subject to noise (reflections on bubbles/droplets), an *ad hoc* filtering technique was implemented. The indicator function was used to filter regions with high image gradients (edge detection) and to mask information with a low signal-to-noise ratio. An illustrative example of the technique is given in Appendix A. The filtered data represented the foreground movement of air-water interfaces throughout the air-water mixture, for example air-bubble interfaces at low void fractions and water-droplet interfaces at high void fractions. The filtering relied on the intensity gradient magnitude, which was calculated as follows

$$\partial \mathbf{I} / \partial x = \mathbf{I} * [-0.5 \ 0 \ 0.5] \quad (7)$$

$$\partial \mathbf{I} / \partial y = \mathbf{I} * \begin{bmatrix} -0.5 \\ 0 \\ 0.5 \end{bmatrix} \quad (8)$$

$$|\nabla \mathbf{I}| = \sqrt{(\partial \mathbf{I} / \partial x)^2 + (\partial \mathbf{I} / \partial y)^2} \quad (9)$$

where \mathbf{I} is the brightness intensity field of the image and $*$ the convolution operator. Optical flow information at an arbitrary location within the image plane was taken into account if the normalised brightness intensity gradient magnitude exceeded an assigned threshold value

$$u \begin{pmatrix} x, y \end{pmatrix}, v \begin{pmatrix} x, y \end{pmatrix} = \begin{cases} u(x, y), v(x, y) & \text{for } |\nabla \mathbf{I}(x, y)| / \overline{|\nabla \mathbf{I}|} \geq g_t \\ \text{discarded} & \text{for } |\nabla \mathbf{I}(x, y)| / \overline{|\nabla \mathbf{I}|} < g_t \end{cases} \quad (10)$$

where u is the streamwise optical flow velocity component, v is the normal optical flow velocity component, $\overline{|\nabla \mathbf{I}|}$ is the spatial and temporal averaged magnitude of the image gradient of the flow field and g_t is the threshold value. Based upon a series of sensitivity tests (Section 5.1), a threshold value $g_t = 1.1$ was chosen to achieve a significantly improved description of the flow and to provide minimum loss of information. The selected value is not unique and represented a conservative choice. A similar procedure should be performed when applying this concept to other flow situations.

4. Measurement results

4.1. Intrusive phase-detection probe measurements

Phase-detection probe measurements provided basic parameters of the air-water flow down the stepped spillway. Measurements were undertaken within the gradually varied flow (GVF) region and represented two characteristic locations, including (1) a profile in between the step edges, characterised by the wake of the step edge and an absence of skin friction and (2) the step edge itself, which acted as a flow singularity [9]. Measurements were performed at the centreline of the channel ($2z/W = 0.0$) and at several transverse positions, including locations at $2z/W = 0.32, 0.95, 0.98$ and 0.996 , corresponding to 335 mm, 25 mm, 10 mm and 2 mm distances to the sidewall, respectively. Measurements next to the sidewall ($2z/W = 0.996$) are marked in blue colour (Fig. 2).

The raw signals of the conductivity probe were analysed by means of a single-threshold technique, yielding void fraction (C), bubble count rate (F) and interfacial velocity (V_c). The void fraction increased with increasing distance from the pseudo-bottom for all measurement locations and exhibited a typical S-shaped profile (Fig. 2A and B). The void fraction was about $C = 0.2$ to 0.4 at the pseudo-bottom between the step edges ($x/L_{\text{cav}} = 5.5$), whereas C was zero at the step edge

($x/L_{\text{cav}} = 6.0$), i.e. at $y = 0$. The transverse profiles indicated the presence of a standing-wave next to the sidewall ($2z/W = 0.98$ and 0.996). The standing-wave appeared to be generated by the impact of the flow onto the tread of the steps, representing a conversion from kinetic energy to potential energy [30].

The number of bubbles next to the pseudo-bottom of the spillway was small at the step edge and increased with increasing y/d_c , whereas the bubble count rate between the step edges had the highest value at the pseudo-bottom and decreased with further distance from the invert (Fig. 2C and D). Note that bubble count rate F was normalised with the critical flow depth d_c and the critical velocity $U_c = \sqrt{gd_c}$. Within the upper flow region, the bubble count rate was small as the probe tips were only hit by few ejected droplets and both cross-sectional profiles were in agreement. The bubble count rates next to the sidewall showed a defect compared to the centreline measurements, confirming sidewall effects.

The distributions of interfacial velocities followed a power-law profile (Fig. 2E and F). Some sidewall effects were observed and velocities next to the wall ($2z/W = 0.996$) showed lower values by about $\pm 10\%$ when compared to centreline data. The velocity deviation was not consistent across the water column due to the sidewall wave and the resulting complicated flow structure. Overall, the sidewall effects appeared to be slightly lower compared to those observed in earlier studies [21,24,32].

4.2. Optical flow measurements

An image sequence of the air-water flow down the stepped chute was recorded for a sampling duration of 11.8 s at a frame rate of 5 kHz (overall 59,000 frames). The high-speed camera was focussed on step cavity 6 (step edges 5–6) and the pixel density was 35 px/cm (Table 2). Fig. 3A shows a snapshot of the air-water mixture with entrained air-bubbles (step cavity) and water-droplets/splashing in the upper region of the flow. The normalised image gradient magnitude had highest values at air-water interfaces in the foreground of the image and low values in monophasic flow regions and regions with blurred background motion (Fig. 3B).

4.2.1. First order flow statistics and indicator function

Optical flow estimates were computed using the Farnebaeck [13] method for an averaging filter-size of 15 pixels and a neighbourhood-size of 5 pixels. An image pyramid multi-resolution approach with three pyramid levels was used [5,6]. The time-averaged streamwise optical flow velocity \bar{u} was calculated as

$$\bar{u} = \frac{1}{t_{s,OF}} \int_{t=0}^{t_{s,OF}} u(t) dt \quad (11)$$

where $t_{s,OF}$ is the sampling duration and u is the instantaneous optical flow velocity.

The optical flow velocity within the step cavity was small and increased with further distance from the invert (Fig. 4A, no filtering). As previously observed, a decrease in optical flow velocity was apparent within the upper flow region [4,3,32], which was in contrast to the phase-detection probe measurements (Fig. 2). Fig. 4B examines the streamwise optical flow field using the indicator function. The optical flow velocity within the step cavity was similar to the velocity field obtained without filtering, but the results showed a significant improvement within the upper flow region. In this region, the velocity profile appeared smooth and no velocity decrease was observed. It is acknowledged that droplets and liquid films, which sometimes attached to the inner surface of the channels sidewall, may have caused some optical flow errors within the upper region.

The normal optical flow velocity fields demonstrated the impact of the flow onto the treads of the steps, generating a cavity recirculation, and they were almost independent of the filtering technique (Fig. 4C and D). Vector plots of velocity fields with and without indicator

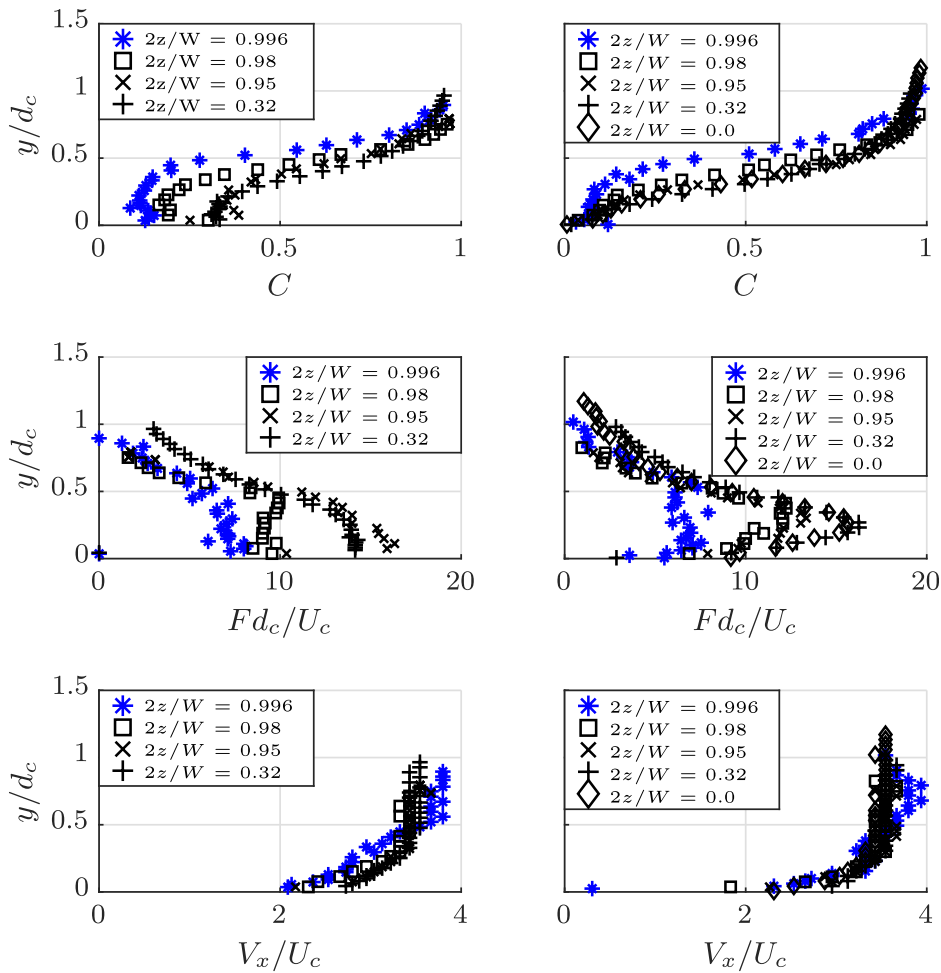


Fig. 2. Intrusive phase-detection probe measurements - comparison of void fraction, bubble count rate and streamwise velocities at different longitudinal and transverse locations; $t_{s,CP} = 90$ s; $f_{s,CP} = 20$ kHz; $d_c/h = 0.8$; $Re = 2.7 \times 10^5$; $\theta = 45^\circ$. (A, top, left) Void fraction distribution between step edges; $x/L_{cav} = 5.5$. (B, top, right) Void fraction distributions at the step edge; $x/L_{cav} = 6.0$ (step edge). (C, middle, left) Bubble count rate between step edges; $x/L_{cav} = 5.5$. (D, middle, right) Bubble count rate at the step edge; $x/L_{cav} = 6.0$ (step edge). (E, bottom, left) Interfacial velocity distribution between step edges; $x/L_{cav} = 5.5$. (F, bottom, right) Interfacial velocity distribution at the step edge; $x/L_{cav} = 6.0$ (step edge).

function are examined in Fig. 4E and F. For clarity, only every 40th vector was taken into account. The velocity fields represented characteristic features of the transition flow regime, including the stagnation point on the horizontal step surface, the recirculation vortex in the step cavity and an almost parallel flow above the pseudo-bottom. Differences in optical flow calculations with and without filtering were also seen.

Using the indicator function, the raw data were filtered mainly within three different regions: the step cavity, the upper flow region and the shear layer (Fig. 4H). This was physically-reasonable as particles (bubbles and droplets) were not always apparent within the cavity

and within the upper region during the measurement period. The shear layer on the image plane showed some particle reflections and those erroneous data were efficiently removed. Even scratches and stains on the sidewall of the channel were recognised by the indicator function (Fig. 4H). In contrast, all 59,000 frames were processed without filtering and the number of removed was equal to zero (Fig. 4G).

4.2.2. Probability density functions of streamwise velocities

To provide a better insight into the mechanism of the indicator function, probability density functions (PDF) of streamwise optical flow velocity estimates are presented ($x/L_{cav} = 5.5$). The streamwise optical

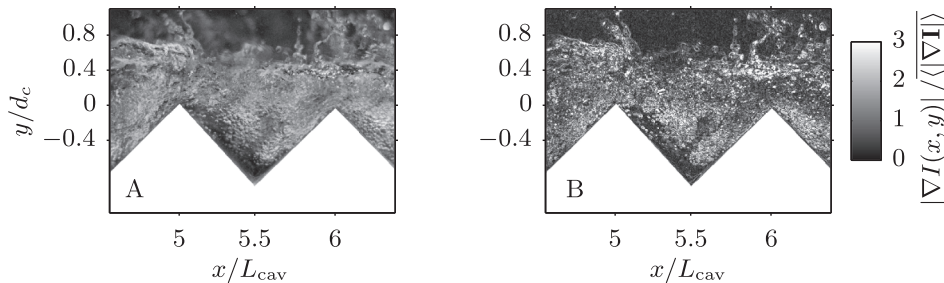


Fig. 3. High-speed image of the air-water flow down the stepped spillway; camera focussed on step cavity 6; flow direction from left to right; $\rho_{px} = 35$ px/cm; $d_c/h = 0.8$; $Re = 2.7 \times 10^5$; $\theta = 45^\circ$. (A, left) Original video frame; camera rotated by 45° . (B, right) Normalised image gradient magnitude.

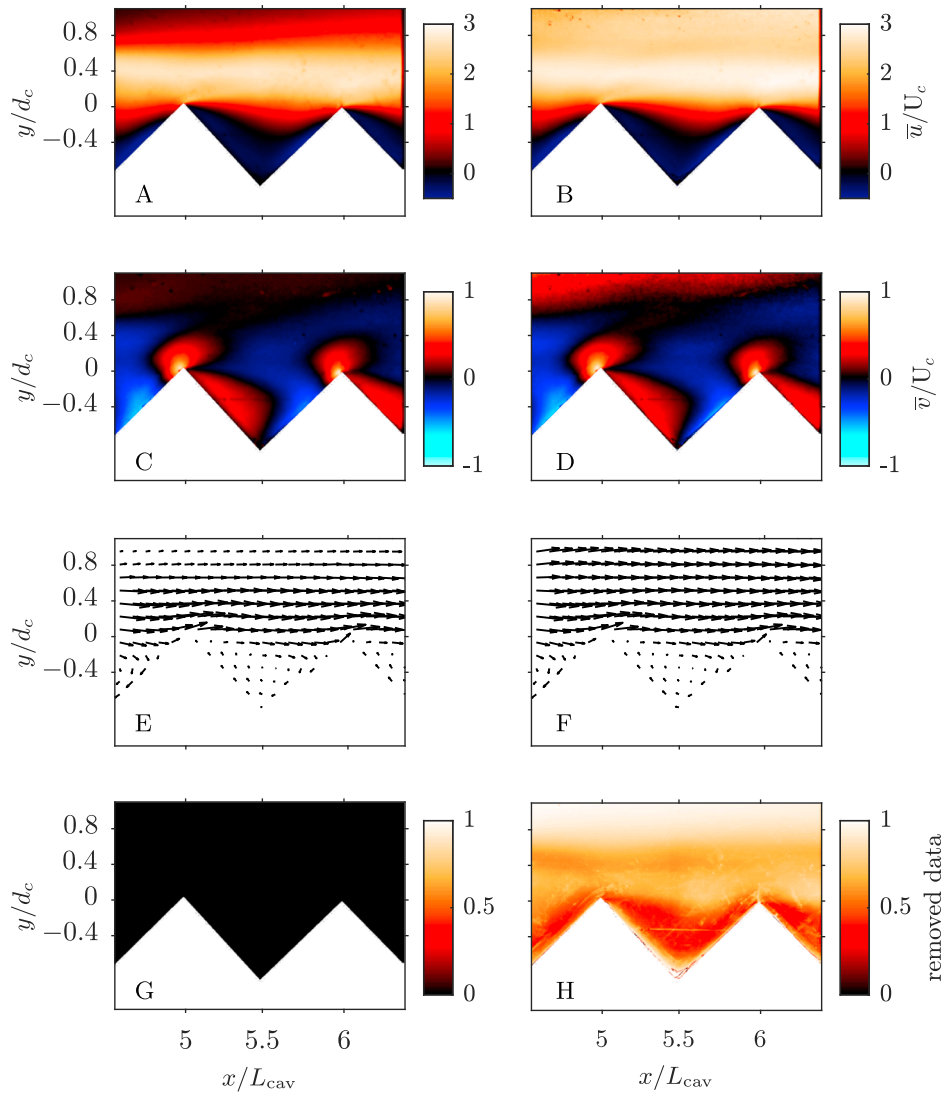


Fig. 4. Effect of the indicator function on optical flow measurements; camera focussed on step cavity 6; flow direction from left to right; $t_{s,OF} = 11.8$ s; $f_{s,OF} = 5$ kHz; $\rho_{px} = 35$ px/cm; $d_c/h = 0.8$; $Re = 2.7 \times 10^5$; $\theta = 45^\circ$. (A) Time-averaged streamwise optical flow velocity field; no filtering. (B) Time-averaged streamwise optical flow velocity field; $g_t = 1.1$. (C) Time-averaged normal optical flow velocity field; no filtering. (D) Time-averaged normal optical flow velocity field; $g_t = 1.1$. (E) Vector plot of the time-averaged velocity field; no filtering. (F) Vector plot of the time-averaged velocity field; $g_t = 1.1$. (G) Amount of removed data, no filtering. (H) Amount of removed data, $g_t = 1.1$.

flow data was normalised by the mean and the standard deviation, and two different elevations ($y/d_c = 0.4$ and $y/d_c = 0.8$) were selected as representative points for the intermediate region ($0.3 < C < 0.7$) and the spray region ($C > 0.7$).

Fig. 5A and B examine the optical flow velocity distributions at an elevation of $y/d_c = 0.8$. The number of processed samples is indicated for each investigated point within the caption of Fig. 5. Without filtering, a bimodal velocity distribution was observed at $y/d_c = 0.8$ (Fig. 5A). Herein, the first and higher mode represented the air-phase, whereas the second mode was much smaller and reflected the optical velocity of the water-phase. The optical flow velocity of the first mode was equal to zero (note that the values are shifted to negative values due to normalisation) as the movement of air was not visible on the image plane. Fig. 5B shows the effect of the gradient threshold on the probability density function at the same elevation. The resulting distribution consisted of 7,111 samples, was similar to a Gaussian and contained interfacial velocities from ejected droplets only. At lower elevations, the indicator function had less effect but still discarded noisy information (Fig. 5C and D). The skewness and the median of the PDF were lower with filtering than without filtering.

4.2.3. Turbulent fluctuations

Optical flow fluctuations were used to characterise the turbulent nature of the air-water flow down the stepped chute. The root-mean-square u'_{rms} of the turbulent optical flow velocity fluctuations was calculated as

$$u'_{rms} = \sqrt{\overline{(u - \bar{u})^2}} \tag{12}$$

Lowest streamwise and normal velocity fluctuations were observed within the recirculation vortex of the step cavity (Fig. 6A and B). The turbulent fluctuations had a local maximum in the shear layer region, linked to the vortex shedding downstream of the step edges associated with high dynamics and turbulence generation.

The turbulence increase in the shear layer is also visible in Fig. 7, where optical flow fluctuations and turbulence intensities are presented between step edges ($x/L_{cav} = 5.5$) and at the step edge ($x/L_{cav} = 6.0$). The two-dimensional turbulence intensity Tu was calculated as

$$Tu = \sqrt{\frac{\frac{1}{2}(\overline{u'^2} + \overline{v'^2})}{\bar{u}^2 + \bar{v}^2}} \tag{13}$$

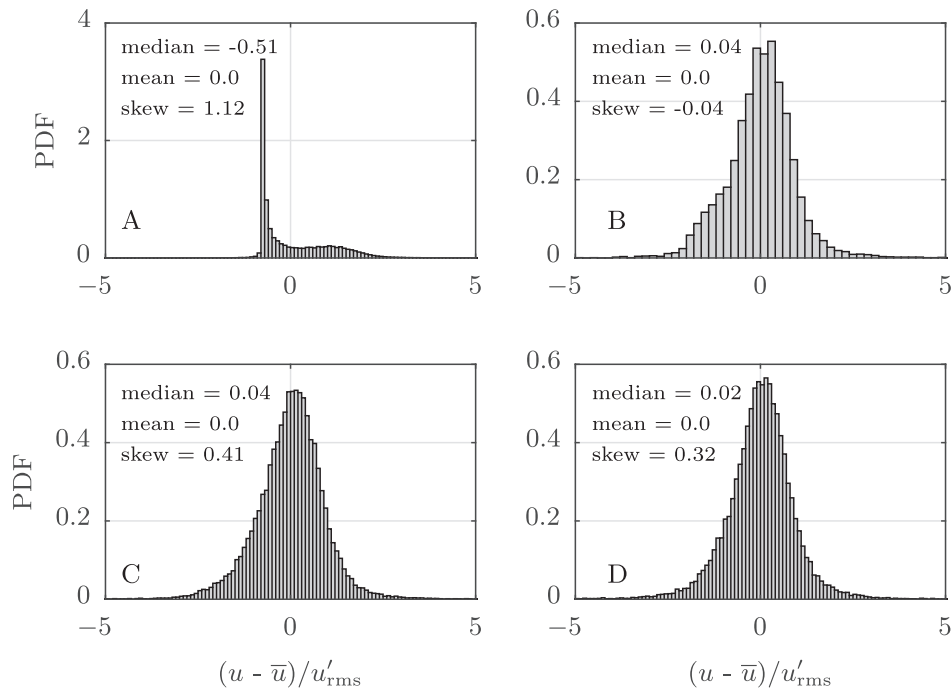


Fig. 5. Probability density functions of streamwise optical flow velocity estimates normalised by the mean and the standard deviation at a longitudinal position of $x/L_{cav} = 5.5$; $t_{s,OF} = 11.8$ s; $f_{s,OF} = 5$ kHz; $\rho_{px} = 35$ px/cm; $d_c/h = 0.8$; $Re = 2.7 \times 10^5$; $\theta = 45^\circ$. (A, top, left) $y/d_c = 0.8$; no filtering; $n = 59,345$. (B, top, right) $y/d_c = 0.8$; $g_t = 1.1$; $n = 7,111$. (C, bottom, left) $y/d_c = 0.4$; no filtering; $n = 59,345$. (D, bottom, right) $y/d_c = 0.4$; $g_t = 1.1$; $n = 23,936$.

As one moves in vertical direction away from the shear region, the turbulent fluctuations were locally decreasing and then increasing towards the spray region (Fig. 7A). The turbulence intensity above the pseudo-bottom ($y/d_c > 0$) was almost constant and ranging between $0.33 < Tu < 0.55$. Fig. 7A shows a distinct peak of the turbulence intensity within the step cavity. These high intensities resulted from low values of the time-averaged optical flow velocity field near the core of the recirculation vortex. At the step edge, a monotonic increase of the turbulent fluctuations along the vertical was observed (Fig. 7B). Note that optical flow data in the upper region with $C > 0.5$ were anticipated to be less accurate compared to the lower region ($C < 0.5$), which was due to variations in brightness intensity, caused by free-surface dynamics.

Overall, the highest turbulent fluctuations occurred within the upper region of the flow. These fluctuations might have been caused by free surface instabilities together with primary breakup and droplet ejection. Further, the normal fluctuations followed the characteristic course of the streamwise fluctuations, albeit being consistently smaller, corresponding to some turbulence anisotropy.

5. Discussion

5.1. Validation of optical flow measurements

To validate the optical flow method, a comparison with intrusive phase-detection probe measurements is presented (Fig. 8). The void fraction distributions (blue lines) were added and only phase-detection probe measurements next to the sidewall were taken into consideration.

The results of the optical flow calculations without filtering showed some significant deviations, especially within the upper flow region, when compared to the phase-detection probe measurements. It is believed that these deviations were primarily caused by (1) image noise and low intensity gradients and (2) inclusion of non-interfacial information. The effect of filtering on the streamwise velocity profiles was studied by varying the threshold of the indicator function. The implementation of the filtering technique led to a significant improvement of the optical flow results, especially in regions with higher void fractions (Fig. 8A and B). In this context, it is pointed out that (1) a further threshold increase above $g_t = 2.3$ did not change the optical flow fields, (2) the number of processed samples decreased with higher thresholding, leading to a higher scatter of the optical flow data.

Relative deviations between streamwise optical flow velocities

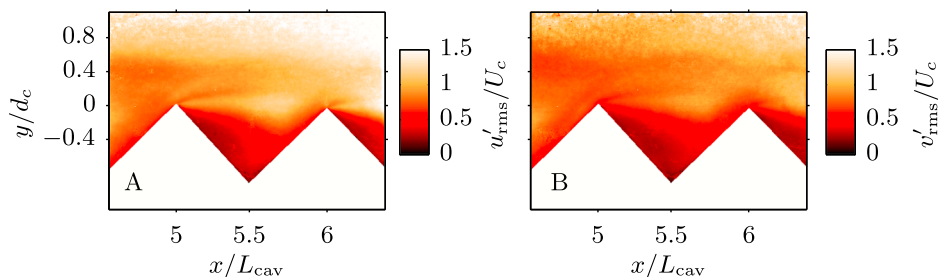


Fig. 6. Time-averaged root mean square of optical flow velocity fluctuations; flow direction from left to right; $t_{s,OF} = 11.8$ s; $f_{s,OF} = 5$ kHz; $d_c/h = 0.8$; $Re = 2.7 \times 10^5$; $\theta = 45^\circ$; $g_t = 1.1$. (A, left) Streamwise optical flow velocity fluctuations. (B, right) Normal optical flow velocity fluctuations.

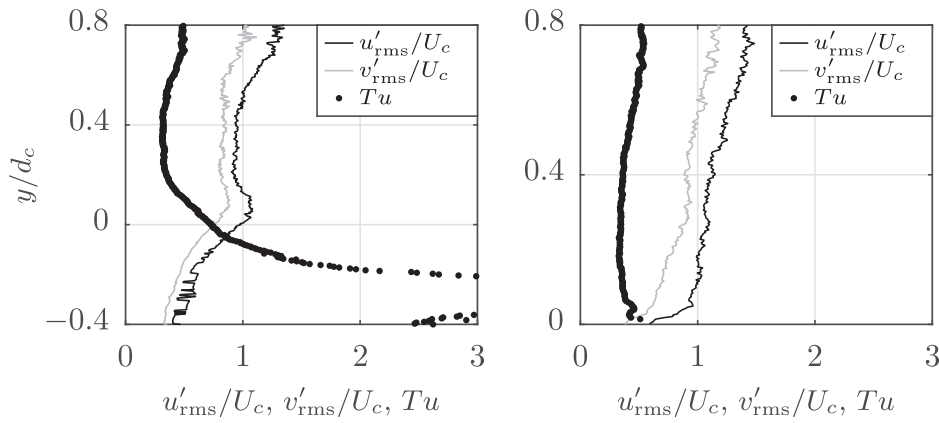


Fig. 7. Profiles of dimensionless time-averaged root mean square optical flow velocity fluctuations and turbulence intensities; $t_{s,OF} = 11.8$ s; $f_{s,OF} = 5$ kHz; $\rho_{px} = 35$ px/cm; $d_c/h = 0.8$; $Re = 2.7 \times 10^5$; $\theta = 45^\circ$; $g_t = 1.1$. (A, left) Instantaneous flow features at $x/L_{cav} = 5.5$ (between step edges). (B, right) Instantaneous flow features at $x/L_{cav} = 6.0$ (step edge).

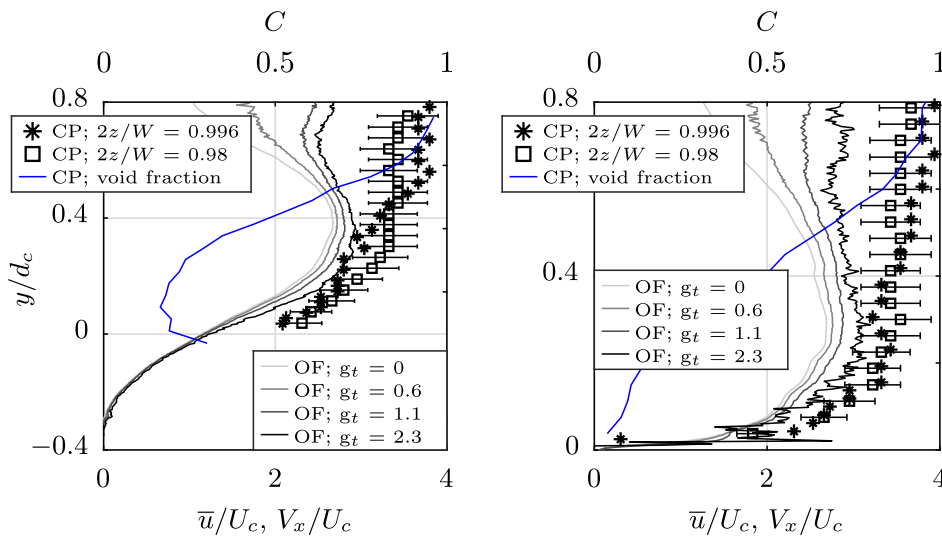


Fig. 8. Validation of optical flow (OF) measurements; time-averaged velocity profiles at different longitudinal locations; \bar{u} : optical flow velocities; V_x : interfacial velocities measured with the phase-detection conductivity probe (CP, including error bars of $\pm 10\%$); C: void fraction; $t_{s,CP} = 90$ s; $f_{s,CP} = 20$ kHz; $t_{s,OF} = 11.8$ s; $f_{s,OF} = 5$ kHz; $d_c/h = 0.8$; $Re = 2.7 \times 10^5$; $\theta = 45^\circ$. (A, left) Streamwise velocity distribution at $x/L_{cav} = 5.5$ (between step edges). (B, right) Streamwise velocity distribution at $x/L_{cav} = 6.0$ (step edge).

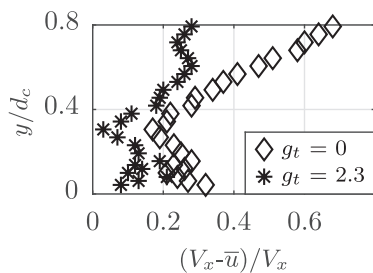


Fig. 9. Relative deviations between streamwise optical flow velocity estimates and phase-detection probe interfacial velocities at the sidewall ($2z/W = 0.996$); $x/L_{cav} = 6.0$ (step edge).

($g_t = 2.3$) and phase-detection probe measurements at the sidewall ($2z/W = 0.996$) were ranging from 5% to 25%, being highest at elevations $y/d_c > 0.4$ (Fig. 9). In the upper region, the flow was sometimes detached from the sidewall, resulting in a ‘smearing’ of liquid films at the inner surface, which led to errors in the optical flow calculations. Without the indicator function ($g_t = 0$), relative deviations up to 70% were observed (Fig. 9, upper flow region).

Overall, there was reasonable agreement between the optical flow

technique and the phase-detection probe when taking the restrictions and uncertainties of the particular instrumentation into account. The highest deviations were found in the upper flow region, where the optical flow technique had difficulties due to processing of background movement and the detached nature of the flow.

5.2. Sensitivity analysis of optical flow estimates

A sensitivity analysis of key sampling and processing parameters was focussed on time-averaged flow statistics to allow systematic comparison with the phase-detection probe data. It is emphasised that the setting of sampling and processing parameters might also have implications for the calculation of second order flow statistics, as demonstrated by Zhang and Chanson [32]. The sensitivity of optical flow measurements with regard to the pixel density was discussed in Bung and Valero [3].

The present analysis was performed with a reference set of parameters, including a neighbourhood-size of 5 pixels, an averaging filter-size of 15 pixels, an image pyramid with three levels and an indicator function with a threshold of $g_t = 1.1$. Consequently, one parameter of the initial set was altered while the rest of the parameters was kept at the reference value. Note that all following results are presented with the filtering method, but

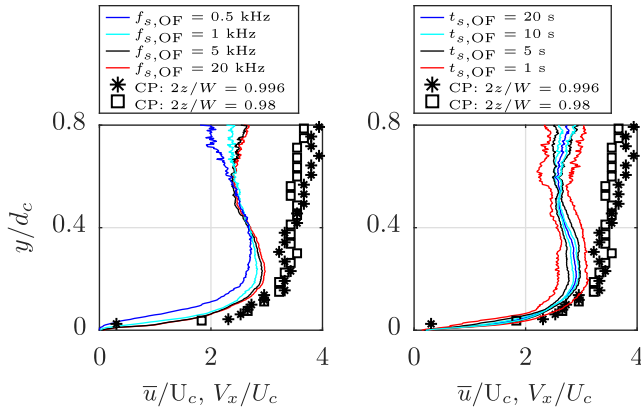


Fig. 10. Effect of video sampling parameters on optical flow (OF) velocity estimates at different longitudinal locations; $\rho_{\text{px}} = 25$ px/cm; $d_c/h = 0.8$; $Re = 2.7 \times 10^5$; $\theta = 45^\circ$; $g_t = 1.1$; $x/L_{\text{cav}} = 6.0$ (step edge) - comparison with phase-detection conductivity probe data (CP). (A, left) Sampling rate and streamwise optical flow velocity. (B, right) Sampling duration and streamwise optical flow velocity.

qualitatively similar trends were observed without filtering.

5.2.1. Sampling rate

The sensitivity of the optical flow method with regard to the sampling rate was tested upon an image sequence with a sampling rate of 20 kHz, subsampled at 5 kHz, 1 kHz and 0.5 kHz (Table 2). The streamwise optical flow velocity component showed highest deviations compared to the conductivity phase-detection probe measurements at sampling rates of 0.5 kHz and 1 kHz (Fig. 10A). The optical flow estimates were converging at sampling rates higher than 5 kHz. Relative deviations between optical flow velocities ($g_t = 1.1$) and phase-detection probe measurements ($2z/W = 0.996$) were ranging from 10% (near pseudo-bottom) to 30% (upper flow region) for sampling rates above 5 kHz, and from 15% to 50% for 0.5 kHz, respectively. Overall, the results were in accordance with an earlier study of Zhang and Chanson [32], where a video sampling rate of $f_{s,\text{OF}} > 5$ kHz (or 5,000 fps) was recommended.

5.2.2. Sampling duration

The optical flow calculations were expected to be dependent on the sampling duration of the recorded image sequence, similar to the

sensitivity of intrusive phase-detection probe measurements. A video sequence with a duration of 20 s (Table 2) was divided into segments of 10 s, 5 s, 1 s. The optical flow calculations were performed for 20 single segments at a sampling duration of 1 s, while four segments were calculated for 5 s and two segments for 10 s. Only maximum and minimum values are shown for durations of 1 s and 5 s (Fig. 10B). A significant scatter of the optical flow data was observed for short sampling durations. The scattering was due to droplets stuck on the inner surface of the glass wall and was decreasing with increasing sampling duration. For sampling durations $t_{s,\text{OF}} \geq 10$ s, relative deviations between OF and CP (sidewall) were ranging from 10% (near pseudo-bottom) to 30% (upper flow region), while deviations between 25% and 45% were observed for 1 s (left curve of Fig. 10B, minimum values). Overall, a minimum sampling duration of $t_{s,\text{OF}} = 10$ s is recommended, but higher durations are highly desirable in terms of more accurate and reproducible results.

5.2.3. Neighbourhood- and filter-size, image pyramid level

The neighbourhood- and the filter-size were varied for values of $N = 1$ px, 2 px, 5 px, 7 px and $F = 5$ px, 10 px, 15 px and 20 px. Herein, one pixel on the image plane corresponded to a physical length of 0.29 mm. A smaller neighbourhood-size resulted in a more accurate prediction of the velocity profiles (when compared to the phase-detection probe data) and the optical flow results converged for neighbourhood-sizes lower than 5 px (Fig. 11A). This behaviour might be explained with the presence of noise within the original image sequence and was likely related to the size of bubbles/droplets. In contrast, a greater filter-size led to a better prediction of the flow velocity profiles (Fig. 11B) and the optimum filter-size was ranging between 10 px and 15 px. Relative deviations between OF and CP (sidewall) in terms of neighbourhood- and filter-sizes were in an order of 10% (near pseudo-bottom) and 30% (upper flow region) for $N \leq 5$ px and $F \geq 10$ px, respectively.

The optical flow velocity profiles did not show a dependence on the number of image pyramid levels and all optical flow data were identical (Fig. 11C). This was in contrast to an earlier investigation of Bung and Valero [6], who applied the Farnebaeck method to synthetic velocity fields. In the present study, no differences were noticeable because the displacements were one order of magnitude smaller than those in the study of Bung and Valero [6].

To summarise, it was appropriate to use a neighbourhood-size between $1 \text{ px} \leq N \leq 5 \text{ px}$ and a filter-size between $10 \text{ px} \leq F \leq 15 \text{ px}$, whereas the implication of the multi-resolution approach did not show

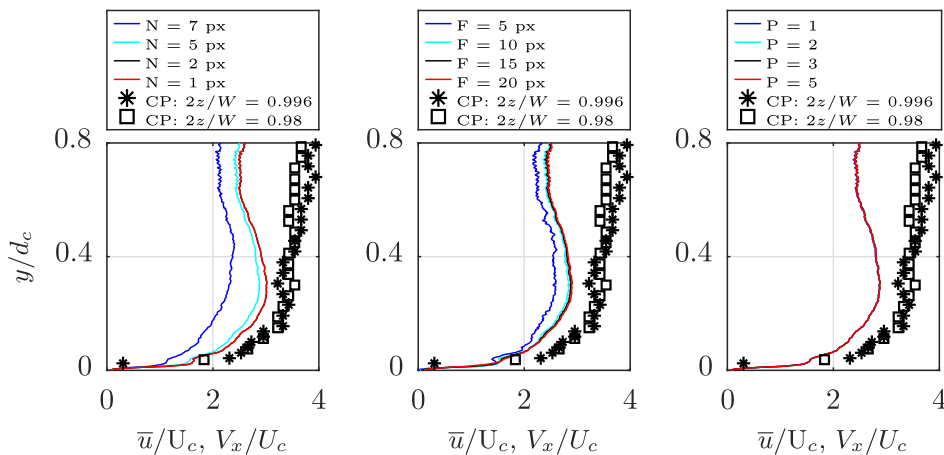


Fig. 11. Effect of processing parameters on optical flow (OF) velocity estimates at different longitudinal locations; $t_{s,\text{OF}} = 11.8$ s; $f_{s,\text{OF}} = 5$ kHz; $\rho_{\text{px}} = 35$ px/cm; $d_c/h = 0.8$; $Re = 2.7 \times 10^5$; $\theta = 45^\circ$; $g_t = 1.1$; $x/L_{\text{cav}} = 6.0$ (step edge) - comparison with phase-detection conductivity probe data (CP). (A, top, left) Neighbourhood-size and streamwise optical flow velocity. (B, top, right) Filter-size and streamwise optical flow velocity. (C, bottom) Image pyramid level and streamwise optical flow velocity.

major benefits. In this context, it is pointed out that the processing parameters are sensitive to the flow situation and always have to be chosen in accordance with the constraints of the recorded image sequence. In the present case, this included absolute flow velocities of around 3 m/s, a video sampling rate of 5 kHz and a pixel density of 35 px/cm.

6. Conclusion

Non-intrusive image-based techniques may allow for estimation of air-water flow velocity fields with a high spatial and temporal resolution. To improve the interpretation of image-based results, the current study presented a systematic comparison of intrusive phase-detection probe measurements with optical flow measurements, undertaken in a large-size physical model of a stepped spillway.

It was shown that the optical flow was representative for the velocity field within the step cavity and the implementation of a new processing technique led to a substantial improvement of the image-based results by about 50% in the upper flow region, when compared to phase-detection probe data. The novel indicator function was used to filter interfacial foreground motion, with potential for further applications in air-water flows. A sensitivity analysis was conducted to determine optimum sampling and processing parameters of the optical flow (Farneback) method. The analysis provided recommendations for

a range of parameters, for example in terms of sampling rate (≥ 5 kHz) and sampling duration (≥ 10 s).

Overall, the study contributes towards the advancement of non-intrusive image-based velocimetry techniques applied to highly-aerated flows. It is anticipated that these techniques will enhance the fundamental knowledge of turbulent properties. Despite the achieved improvements, some deviations remained, and it is believed that these deviations were mainly due to the detached nature of the flow. Future research could focus on shadowgraphy techniques to reduce light reflections of bubbles/droplets and consequently increase the signal-to-noise ratio.

Conflict of interest

The authors declare that there are no conflicts of interest.

Acknowledgements

The authors thank Jason Van Der Gevel and Stewart Matthews (The University of Queensland) for the technical assistance. They gratefully acknowledge Daniel Valero (FH Aachen) and Gangfu Zhang (The University of Queensland) for the helpful discussions. Matthias Kramer was supported by DFG Grant No. KR 4872/2-1.

Appendix A. Indicator function

The indicator function is an *ad hoc* filtering technique which works on the image plane. The advantages of this technique include (1) removal of erroneous data (2) filtering of air-water interfaces (3) filtering of foreground movement. A simple example is presented to demonstrate the working principle. Herein, a synthetic image I_1 (400×400 pixels) with a random pattern of 400 particles was generated. The particles had a uniform diameter of 10 pixels and a brightness intensity of 255 (Fig. 12A). The gradient magnitude of I_1 was calculated based on a central-differences scheme. Similar to an edge detection filter, the particle edges constituted the highest values of the gradient magnitude (Fig. 12C).

A streamwise translational motion with a defined displacement ($D_x = 4$ pixels) was imposed, leading to I_2 (Fig. 12B). Subsequently, the optical flow between I_1 and I_2 was calculated using the Farneback method ($F = 5$ px), where the pixelwise solution was integrated over a specific neighbourhood $N = 5$ pixels. Estimation errors were observed within the neighbourhood of the particles and near the image border (Fig. 12D). These errors were also seen in the probability density function (PDF), reflecting some underestimation of measured displacements in streamwise direction (Fig. 12E).

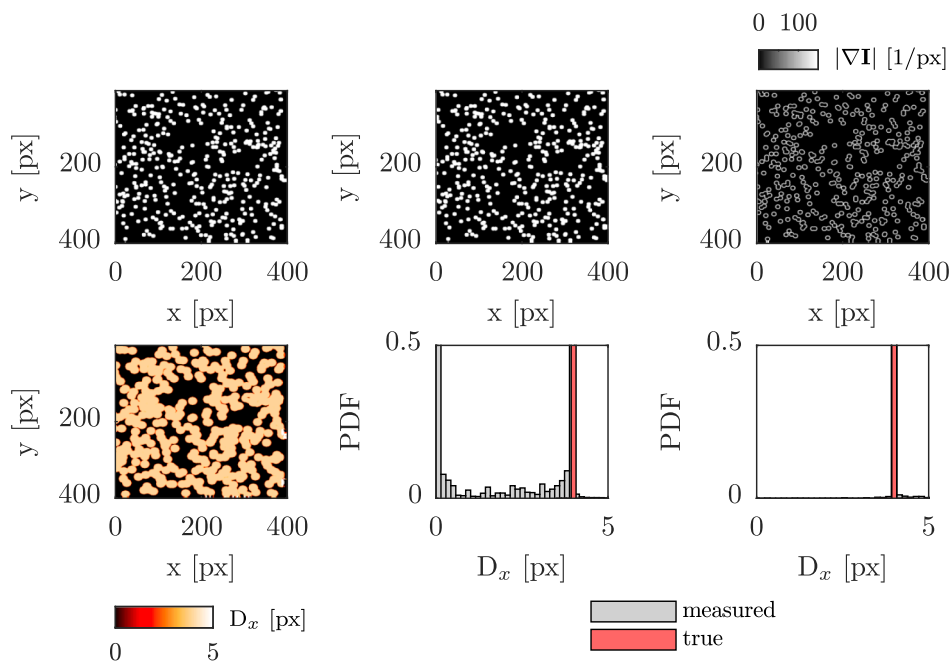


Fig. 12. Indicator function applied to synthetic images. (A, top, left) Synthetic particle image I_1 . (B, top, middle) Synthetic particle image I_2 after displacement; $D_x = 4$ px. (C, top, right) Image gradient magnitude of I_1 . (D, bottom, left) Streamwise optical flow between I_1 and I_2 . (E, bottom, middle) PDF of streamwise displacements. (F, bottom, right) PDF of streamwise displacements - indicator function.

The indicator function was applied to the optical flow calculation. The image gradient magnitude within the synthetic image had 3 values (0, 127.5 and 183.3) and only displacements of pixels with values $|\nabla I| = 127.5$ and 183.3 were evaluated. After filtering, the PDF (Fig. 12F) demonstrated that erroneous data were efficiently removed and that only the motion of particle edges (i.e. air-water interfaces) was taken into account.

References

- [1] J.L. Barron, D.J. Fleet, S.S. Beauchemin, Performance of optical flow techniques, *Int. J. Comput. Vision* 12 (1994) 43–77.
- [2] R.M. Boes, *Zweiphasenströmung und Energieumsetzung an Grosskaskaden*, PhD thesis, ETH Zuerich, 2000.
- [3] D. Bung, D. Valero, Image processing techniques for velocity estimation in highly aerated flows: bubble image velocimetry vs. optical flow, *Proceedings of the 4th IAHR Europe Congress*, Liege, Belgium, 2016, pp. 151–157.
- [4] D.B. Bung, Non-intrusive measuring of air-water flow properties in self-aerated stepped spillway flow, *Proceedings of the 34th IAHR World Congress*, Brisbane, Australia, 2011, pp. 2380–2387.
- [5] D.B. Bung, D. Valero, Optical flow estimation in aerated flows, *J. Hydraul. Res.* 54 (2016) 575–580.
- [6] D.B. Bung, D. Valero, FlowCV - an open source toolbox for computer vision applications in turbulent flows, *E-Proceedings of the 37th IAHR World Congress*, Kuala Lumpur, Malaysia, 2017, 10 pages.
- [7] A. Cartellier, J.L. Achard, Local phase detection probes in fluid/fluid two-phase flows, *Rev. Sci. Instrum.* 62 (2) (1991) 279–303.
- [8] H. Chanson, Air-water flow measurements with intrusive, phase-detection probes: can we improve their interpretation? *J. Hydraulic Eng.* 128 (3) (2002) 252–255.
- [9] H. Chanson, L. Toombes, Hydraulics of stepped chutes: the transition flow, *J. Hydraulic Eng.* 42 (1) (2004) 43–54.
- [10] T. Corpetti, D. Heitz, G. Arroyo, E. Mémin, A. Santa-Cruz, Fluid experimental flow estimation based on an optical-flow scheme, *Exp. Fluids* 40 (1) (2006) 80–97.
- [11] P.D. Cummings, H. Chanson, Air entrainment in the developing flow region of plunging jets - part 2: experimental, *J. Fluids Eng.* 119 (3) (1997) 603–608.
- [12] G. Farnebaeck, *Polynomial expansion for orientation and motion estimation*, PhD thesis, University of Linköping, 2002.
- [13] G. Farnebaeck, Two-frame motion estimation based on polynomial expansion, *Proceedings of the 13th Scandinavian Conference on Image Analysis*, Halmstad, Sweden, 2003, pp. 363–370.
- [14] S. Felder, H. Chanson, Phase-detection probe measurements in high-velocity free-surface flows including a discussion of key sampling parameters, *Exp. Thermal Fluid Sci.* 61 (2015) 66–78.
- [15] D. Fortun, P. Boutheymy, C. Kervrann, Optical flow modeling and computation: a survey, *Comput. Vis. Image Underst.* 134 (2015) 1–21.
- [16] V.M. Govindu, Revisiting the brightness constraint: probabilistic formulation and algorithms, *Computer Vision ECCV 2006. Lecture Notes in Computer Science*, Graz, Austria, 2006, pp. 177–188.
- [17] D. Heitz, E. Mémin, C. Schnörr, Variational fluid flow measurements from image sequences: synopsis and perspectives, *Exp. Fluids* 48 (3) (2010) 369–393.
- [18] R.A. Herringe, M.R. Davis, Structural development of gas-liquid mixture flows, *J. Fluid Mech.* 73 (1) (1976) 97–123.
- [19] B.K. Horn, B. Schunck, Determining optical flow, *Artif. Intell.* 17 (1981) 185–203.
- [20] O.C. Jones, J.-M. Delhay, Transient and statistical measurement techniques for two-phase flows: A critical review, *Int. J. Multiph. Flow* 3 (1975) 89–116.
- [21] K. Kramer, *Development of Aerated Chute Flow*, PhD thesis, ETH Zurich, 2004.
- [22] M. Kramer, H. Chanson, Free-surface instabilities in high-velocity air-water flows down stepped chutes, 7th International Symposium on Hydraulic Structures (ISHS 2018), Aachen, Germany, 2018 11 pages.
- [23] M. Kramer, H. Chanson, Transition flow regime on stepped spillways: air-water flow characteristics and step-cavity fluctuations, *Environ. Fluid Mech.* 18 (2018) 947–965.
- [24] J. Leandro, D.B. Bung, R. Carvalho, Measuring void fraction and velocity fields of a stepped spillway for skimming flow using non-intrusive methods, *Exp. Fluids* (2014) 55.
- [25] T. Liu, A. Merat, M.H.M. Makhmalbaf, C. Fajardo, P. Merati, Comparison between optical flow and cross-correlation methods for extraction of velocity fields from particle images, *Exp. Fluids* 56 (8) (2015) 1–23.
- [26] T. Liu, L. Shen, Fluid flow and optical flow, *J. Fluid Mech.* 614 (2008) 253–291.
- [27] B.D. Lucas, T. Kanade, An iterative image registration technique with an application to stereo vision, *Proceedings of the 7th international joint conference on artificial intelligence*, Vancouver, Canada, 1981, pp. 674–679.
- [28] L.G. Neal, S.G. Bankoff, A high resolution conductivity probe for determination of local void properties in gas-liquid flow, *AIChE J.* 9 (1963) 490–494.
- [29] Y. Ryu, K.A. Chang, H.J. Lim, Use of bubble image velocimetry for measurement of plunging wave impinging on structure and associated greenwater, *Meas. Sci. Technol.* 16 (2005) 1945–1953.
- [30] L. Toombes, *Experimental study of air-water flow properties on low-gradient stepped cascades*, PhD thesis, The University of Queensland, 2002.
- [31] G. Zhang, H. Chanson, Hydraulics of the developing flow region of stepped spillways. I: physical modeling and boundary layer development, *J. Hydraulic Eng.* 142 (7) (2016) 8 pages.
- [32] G. Zhang, H. Chanson, Application of local optical flow methods to high-velocity free-surface flows: validation and application to stepped chutes, *Exp. Therm. Fluid Sci.* 90 (2018) 186–199.